

# Anomalous Epitaxial Growth in Thermally Sprayed YSZ and LZ Splats

Lin Chen<sup>1</sup> · Guan-Jun Yang<sup>1</sup>

Submitted: 15 January 2017 / in revised form: 8 May 2017 / Published online: 13 June 2017  
© ASM International 2017

**Abstract** Thermally sprayed coatings are essentially layered materials, and lamellar interfaces are of great importance to coatings' performances. In the present study, to investigate the microstructures and defect features at thermally sprayed coating interfaces, homoepitaxial 8 mol.% yttria-stabilized zirconia (YSZ) and heteroepitaxial lanthanum zirconia (LZ) films were fabricated. The epitaxial interfaces were examined by high-resolution transmission electron microscope (HR-TEM) in detail. As a result, we report, for the first time, an anomalous incommensurate homoepitaxial growth with mismatch-induced dislocations in thermally sprayed YSZ splats to create a homointerface. We also find the anomalous heteroepitaxial growth in thermally sprayed LZ splats. The mechanism of the anomalous incommensurate growth was analyzed in detail. Essentially, it is a pseudo-heteroepitaxy because of the lattice mismatch between the film and the locally heated substrate, as the locally heated substrate is significantly strained by its cold surroundings. Moreover, the super-high-density dislocations were found in the interfacial region, which resulted from sufficient thermal fluctuations and extremely rapid cooling rates. Both the anomalous lattice mismatch and super-high-density dislocations lead to weak interfaces and violent cracking in thermally sprayed coatings. These were also the essential differences between the conventional and the present epitaxy by thermal spray technique.

**Keywords** cracking · dislocations · epitaxial growth · enormous compressive strain · locally heated substrate

## Introduction

Thermally sprayed coatings have been widely used as thermal barrier coatings (TBCs) (Ref 1, 2), functional layers in solid oxide fuel cells (SOFCs) (Ref 3), wear-resistant coatings (Ref 4), and abradable seal coatings (Ref 5-7). The spraying process characterizes the coatings with a large number of splats piling up layer by layer, which indicates that there exist innumerable lamellar interfaces in thermally sprayed coatings. Obviously, the qualities of the interfaces determine the coating performances such as service life and thermal/electric conduction. As the case with TBCs, it was widely reported that delamination at the lamellar interfaces was the uppermost failure mode during their service stage (Ref 8-10). Besides, it was found that the tens/hundreds of microns long delamination had produced during the coating formation (Ref 11) which acted as the initial crack sources. These preexisting cracks can easily coalesce each other and lead to the final failure during the services. Consequently, combined action of these weak interfaces and thermally grown oxides (TGO) significantly promotes TBC failure. Therefore, tailoring the qualities of these interfaces is also the key to promoting the coating performances.

As we know (Ref 12), there are three general types of interfaces between two solid phases: coherent interface, semicoherent interface and incoherent interface. A coherent interface arises when there is a one-to-one correspondence of atomic planes across the boundaries separating two phases. When the lattice parameter difference

✉ Guan-Jun Yang  
ygj@mail.xjtu.edu.cn

<sup>1</sup> State Key Laboratory for Mechanical Behavior of Materials, School of Materials Science and Engineering, Xi'an Jiaotong University, Xi'an 710049, Shaanxi, People's Republic of China

increases, there is a corresponding increase in coherency strains. Eventually, it becomes energetically more favorable to introduce periodically spaced dislocations to accommodate the misfit, and such interfaces are said to be semicoherent. As to the incoherent interface, it lies between two phases with different crystal structures and thereby much different atomic spacing. Essentially, the main differences among these three types of interfaces come from the quantities and distributions of the defects. Undoubtedly, the defect features dominate the qualities of interfaces. However, much attention was paid to the morphologies and diffraction features of the interfaces in the previous studies (Ref 13–16). A systematical investigation of the quantity and distribution of the defects at the interfaces remains unexplored.

In addition, vertical or transverse cracks are ubiquitous during the deposition process. It was reported that the vertical cracks were mainly due to the quenching stress during the deposition process (Ref 17–19). The value of quenching stress was conventionally measured by curvature method after cracking, which yielded only  $\sim 100$  MPa. However, the quenching stress is generally defined as the stress resulting from the different temperature-changing rates at different positions. As to the thin splat (with thickness of  $\sim 1$   $\mu\text{m}$ ), the temperature differences can be neglected. In addition, the measured stress was only the value after cracking, and the precision of the curvature method was also not high. Therefore, the value and formation mechanism of cracking stress during deposition remain unclear up to now.

In brief, although thermally sprayed technique has been widely used for many years, the defect features at interfaces and the value of cracking stress during the deposition process were hardly concerned.

In the present study, to avoid the influence of grain boundaries and for convenience, the 8 mol.% yttria-stabilized zirconia (YSZ) and lanthanum zirconia (LZ) splats deposited on the single-crystal YSZ substrate were employed. It was found that epitaxial growth readily occurred for all splats at the deposition temperatures of 300 and 600 °C. The microstructures and defect features at these epitaxial interfaces were investigated to elaborate the interface qualities and essential properties of thermally sprayed coatings.

Additionally, the growth of semiconductor films by techniques such as molecular beam epitaxy has proved to be useful in probing the nucleation and growth of defects such as dislocations and cracks as well as surface roughening. All the defects play important roles in stress relaxations of strained epitaxial films. In addition, how to develop and control the defects or strains in materials has obtained wide applications in photocatalysts (Ref 20, 21), biology (Ref 22–24), functional thin films (Ref 25–27) and

nanowires (Ref 28, 29). According to the compositions, there are generally two kinds of epitaxies, namely homoepitaxy (with the same composition between substrate and film) and heteroepitaxy (with the different compositions between substrate and film). Besides, depending upon the extent of the lattice mismatch (Ref 30), epitaxial growth processes can be divided into commensurate (a), pseudomorphic (b) and incommensurate (c), as shown in Fig. 1. Commensurate growth means a perfect lattice match between film and substrate and theoretically can only be possible for homoepitaxy, while pseudomorphic and incommensurate growths are due to the lattice mismatch between the film and the substrate and generally occur for heteroepitaxy. The difference between pseudomorphic and incommensurate growths is that the latter contains large numbers of defects in the film/substrate interfacial region which significantly influence the device properties (Ref 31–34), while the former was widely used to manufacture perfectly flawless heterojunctions (Ref 26, 35). Apparently, commensurate and pseudomorphic growths correspond to coherent interface, while incommensurate corresponds to semicoherent interface. Routinely, traditional homoepitaxy is a slow equilibrium process, which results in a perfect lattice match and thus commensurate growth. However, we report here, for the first time, an anomalous incommensurate growth is also possible for homoepitaxy when a highly non-equilibrium process, thermal spray technique (liquid-phase epitaxy) is adopted. These discoveries are of significant importance and open a door to deeply understand the essential properties of thermally sprayed coatings.

## Experiment

### Materials

In this study, YSZ and LZ, as demonstration materials for TBCs, were employed to explore the microstructures of homointerfaces and heterointerfaces, respectively. The surface morphology of the YSZ and LZ powders is shown in Fig. 2(a) and (b), respectively. The fused-crushed YSZ powder (Fujimi, Japan) had a particle size range from 5 to 25  $\mu\text{m}$  with a mean size of 17.8  $\mu\text{m}$  measured by a laser particle size analyzer (LS230, Beckman Coulter, USA) with a measuring range from 0.04 to 2000  $\mu\text{m}$ , and the particle size of LZ agglomerate powder (Tianyao, Qingdao, China) ranged from 15 to 45  $\mu\text{m}$  with a mean size of 30  $\mu\text{m}$ . All films were deposited on (001) plane of single-crystal YSZ substrate with a well-polished surface, whose arithmetical average error of outlines ( $R_a$ ) was  $<0.5$  nm. The substrates were square, with a width of 10 mm and a

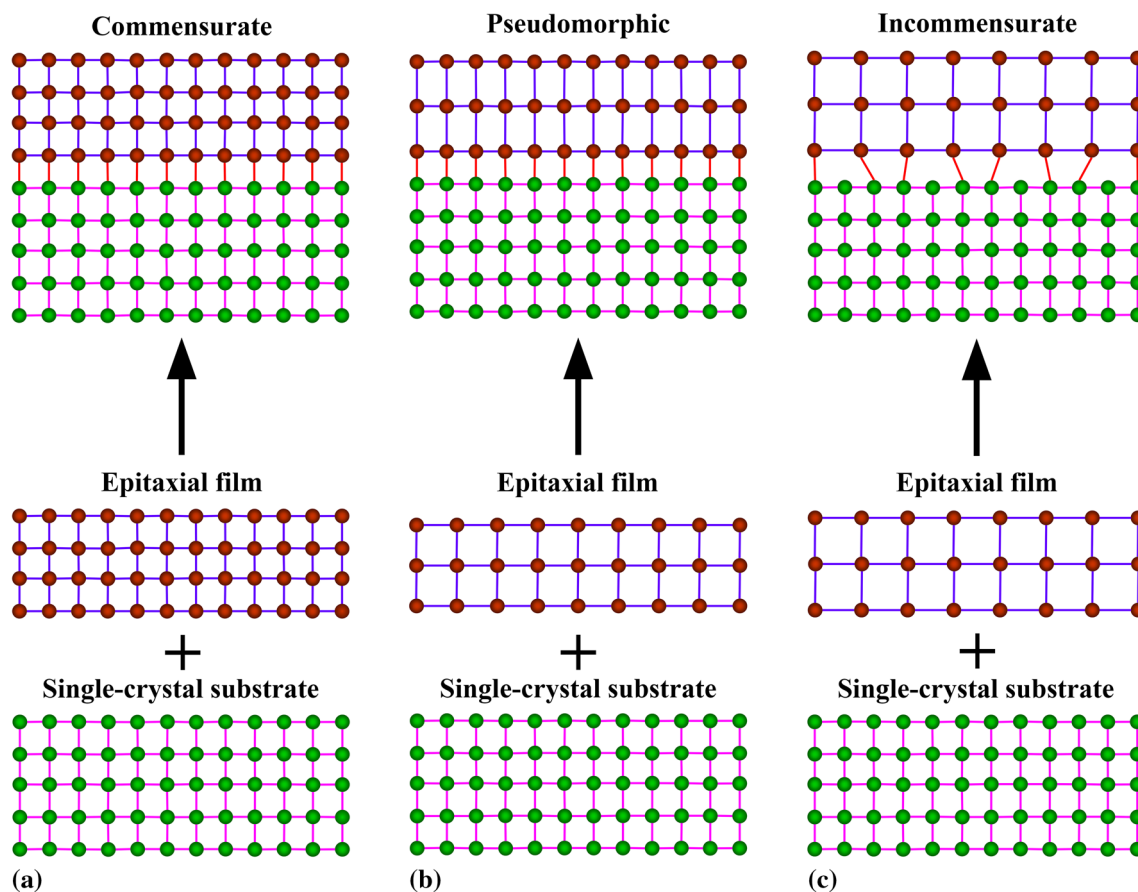


**Fig. 1** A schematic diagram of (a) commensurate, (b) pseudomorphic and (c) incommensurate growth in epitaxy depending upon the extent of the lattice mismatch

thickness of 500  $\mu\text{m}$ . The side faces of the substrate were oriented along  $\langle 100 \rangle$  directions.

### Splat Deposition

A commercial plasma spray system (GP-80, Jiujiang, China) and an external powder feeding injector were employed. The spray power and distance were 42 kW and 80 mm, respectively. Moreover, the traverse speed of torch was set to be 1200 mm/s. The argon (Ar) and hydrogen ( $\text{H}_2$ ) were employed as the primary and secondary plasma gases with the value of 50 and 7 slpm, respectively. The nitrogen ( $\text{N}_2$ ) was selected as the powder feed gas with the value of 3 slpm. Prior to the film deposition, we preheated the substrate to 300 and 600  $^\circ\text{C}$  through a copper plate heater on which the substrates were placed (Ref 36, 37). The temperature was real-time-monitored by a calibrated thermocouple (NiCr/NiCrSi, Type N) and could maintain the set value with a variation less than 10  $^\circ\text{C}$  over a 5-min time interval. In addition, to avoid the extra calefaction of the substrate by plasma arc, a shielding plate with several

small holes was clamped on the substrate. After the splat deposition, the film and substrate were cooled down to room temperature in atmosphere.

### Characterization of Splats

The splats surface morphology was observed by scanning electron microscopy (SEM, VEGA II-XMU, TESCAN, Czech Republic), and the epitaxial growth of the splats was first confirmed by electron backscattered diffraction (EBSD, AZTEC, OXFORD INSTRUMENTS, UK). Moreover, a TITAN (FEI, USA, operating at 350 kV) Cs-corrected high-resolution transmission electron microscope (HR-TEM) was employed to investigate the epitaxial interface in detail. The TEM samples were prepared by focused ion beam (FIB, FEI Quanta 200 FEG, USA). After the FIB preparation, the samples were cleaned by Nano Mill (M1040 Nano Mill, Fischione, USA) to remove the amorphous layers produced by the bombardment of FIB. The argon ion ( $\text{Ar}^+$ ) was selected as cleaning agent. The milling angle and the ion energy were 30 $^\circ$  and 700 eV,

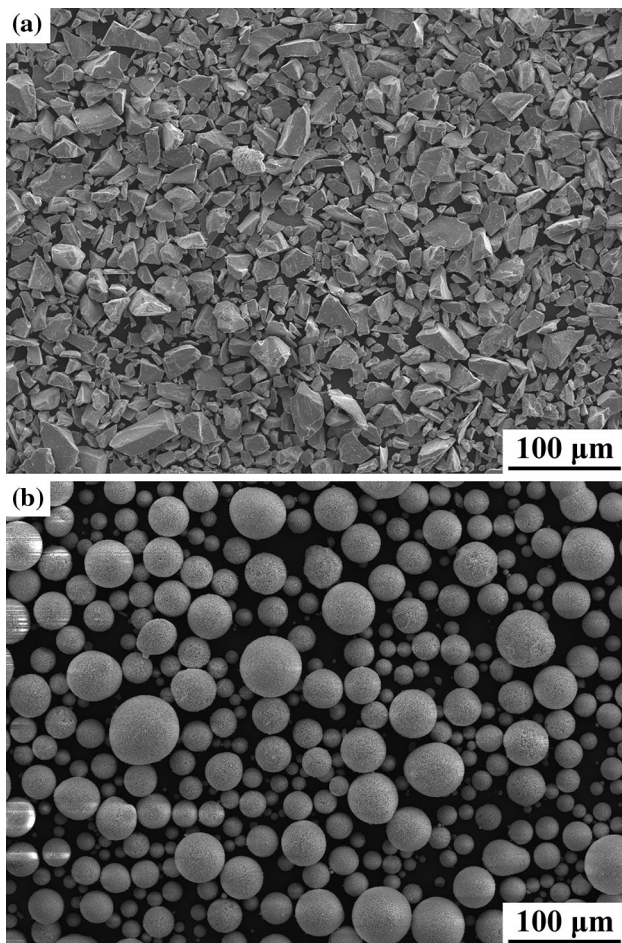


**Fig. 2** Surface morphologies of (a) YSZ fused-crushed and (b) LZ agglomerate powders

respectively. The milling time for every face of the sample was set as 30 min.

## Results

### Surface Morphology of YSZ Splats

The YSZ splats on the single-crystal YSZ substrate presented regular pattern morphologies, as shown in Fig. 3. During SEM observation, the substrate edge was always kept parallel to the edge of the SEM view field. It was found that vertical cracks were generally oriented at  $45^\circ$  angle to the substrate  $\langle 100 \rangle$  direction (side face), which revealed  $\langle 110 \rangle$  orientations for vertical cracks, as shown by the red arrows in Fig. 3(a) and (b). This was consistent with the closest packed direction of face-centered cubic (FCC) structure of YSZ material. Due to regular cracking, an array of nanochannels (see insets in Fig. 3a and b) was successfully fabricated. Quantitative examination results showed that the mean strip width was about 16.5 and

17.8  $\mu\text{m}$  at the deposition temperatures of 300 and 600  $^\circ\text{C}$ , respectively. In addition, substrate delamination already occurred for YSZ splats deposited at both 300 and 600  $^\circ\text{C}$ . The epitaxial growth of the splats was first confirmed by EBSD, as shown in Fig. 3(c) and (d). The inverse pole figures (IPFs, see insets in Fig. 3c and d) indicated the film grew along the  $\langle 001 \rangle$  orientation. The IPFs and identical color between film and single-crystal substrate clearly revealed the epitaxial growth had successfully occurred along the  $\langle 001 \rangle$  direction.

### Surface Morphology of LZ Splats

Similar to the case of YSZ splats, the LZ splats on the single-crystal YSZ substrate also presented regular pattern morphologies, as shown in Fig. 4. All vertical cracks were along  $\langle 110 \rangle$  orientations which were consistent with the closest packed directions of LZ material (FCC structure), as shown by the red arrows in Fig. 4(a) and (b). The mean strip width of LZ splats was about 12.13 and 12.57  $\mu\text{m}$  at the deposition temperatures of 300 and 600  $^\circ\text{C}$ , respectively. In addition, both interface and substrate delamination already occurred for LZ splats deposited at 300  $^\circ\text{C}$  (Fig. 4a), while only substrate delamination occurred at 600  $^\circ\text{C}$  (Fig. 4b). Interestingly, residual vertical cracks were also observed on the bare substrate. As expected, the identical color (Fig. 4c and d) and IPFs (insets in Fig. 4c and d) clearly revealed the epitaxial growth had successfully occurred along the  $\langle 001 \rangle$  direction. Notably, the interface delamination indicated a weak LZ/YSZ interface, which was incompatible with the characteristic of epitaxial growth.

### Statistics of Dislocations at Homoepitaxial YSZ Interfaces

Subsequently, the homoepitaxial YSZ interfaces were examined by a Cs-corrected HR-TEM, as shown in Fig. 5. The film was about 300–500 nm thick (see Fig. 8a and b in “Appendix”). Under high magnification, distinct interface contrasts were observed at the homoepitaxial interface, as shown in Fig. 5(a), (b), (e) and (f). Generally, an opposite contrast on bright-field images (BF-TEM) or dark-field images (DF-TEM) was due to the existing defects. Knowing that the cracks were always along  $\langle 110 \rangle$  directions and to associate the defects with cracking, we conducted fast Fourier transform (FFT, by DigitalMicrograph, Gatan, UK) for the HR-TEM images and then conducted inverse fast Fourier transform (IFFT) only for the diffraction spot with  $g = [220]$  (as shown in Fig. 9 in “Appendix”). As expected, a fair number of defects at the interface were observed from the FFT-IFFT images, as shown in Fig. 5(d) and (h). Except for the stacking faults,

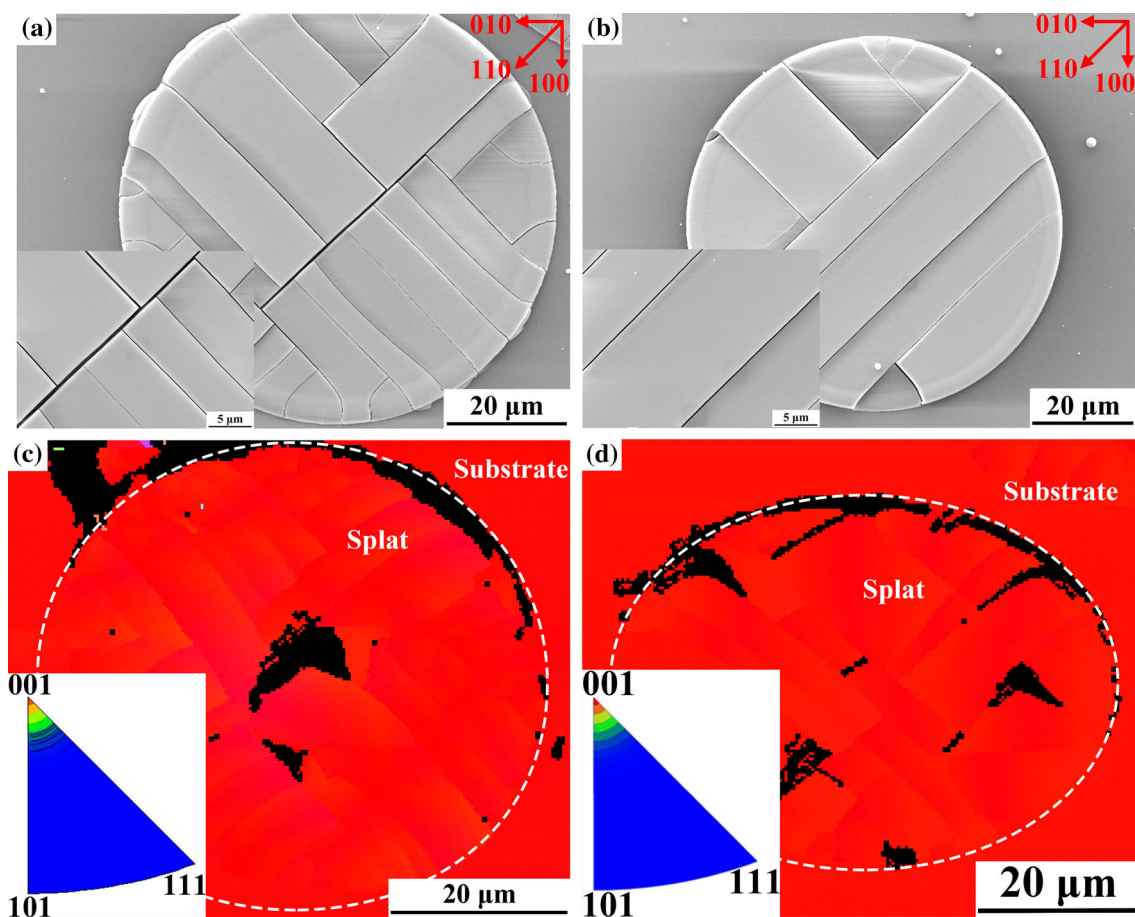


**Fig. 3** Surface morphologies of the YSZ film on the single-crystal YSZ substrate at deposition temperatures of (a) 300 °C and (b) 600 °C. The insets in (a) and (b) correspond to high magnification. The red arrows in (a) and (b) represent the crystal directions. The orientation maps of YSZ films at deposition temperatures of

(c) 300 °C and (d) 600 °C by EBSD. The insets in (c) and (d) correspond to inverse pole figures (IPFs). The red color and IPFs in EBSD patterns indicate the  $\langle 001 \rangle$  orientation. The identical color between film and single-crystal substrate clearly reveals the epitaxial growth has successfully occurred (Color figure online)

many edge dislocations (marked by red signs) with a Burgers vector ( $b$ ) of  $(a/2)\langle 110 \rangle$  were also present in the interfacial region (marked by two pink dashed lines). It was found that the spacing of two closest dislocations is generally no less than  $4b$ . Considering that positive and negative dislocations lead to a contrary local deformation of the crystal lattice, we firstly determined the net dislocations along the interfaces. To quantitatively evaluate and associate the dislocations with the strains in films, the dislocation concentration (Ref 38, 39) was adopted and defined as the ratio of the net dislocations to the total lattice numbers along the epitaxial interfaces. Apparently, the strain relaxed by dislocations was equal to the dislocation concentration. For the calculation, 24 high-magnified images with a total interface length of about 430 nm were used. We found that considerable net dislocations existed in the interfacial region corresponding to the distinct interface contrasts, i.e.,  $1.37 \pm 0.29$  and  $1.08 \pm 0.21\%$  for deposition temperatures of 300 and 600 °C, respectively.

There are generally two types of strain components (Ref 40): one is stress-induced physical strain which obeys Hooke's law. The other is intrinsic strain caused by thermal, electric and magnetic field; and defects (such as dislocations and stacking faults); etc. This kind of intrinsic strain does not generate stress in free condition, such as the free thermal expansion. Based on the definition in elasticity (Ref 40), the total strain is only related to the displacement change. As the case with homoepitaxial growth (namely, the perfect lattice match between the film and substrate), the total strain is equal to zero. Consequently, the physical strain is equal to the intrinsic strain relaxed by two types of defects that exist in the interfacial region: stacking faults and net dislocations. The stacking faults shown in Fig. 5(d) and (h) are always less than 3 nm in size, and the TEM images show no stacking faults going through the whole field. Thus, we can state that all the stacking faults are local defects. Local stacking faults contribute little to the strain relaxation. As a result, the physical strain is only correlated to net dislocations and has the value  $1.37 \pm 0.29$

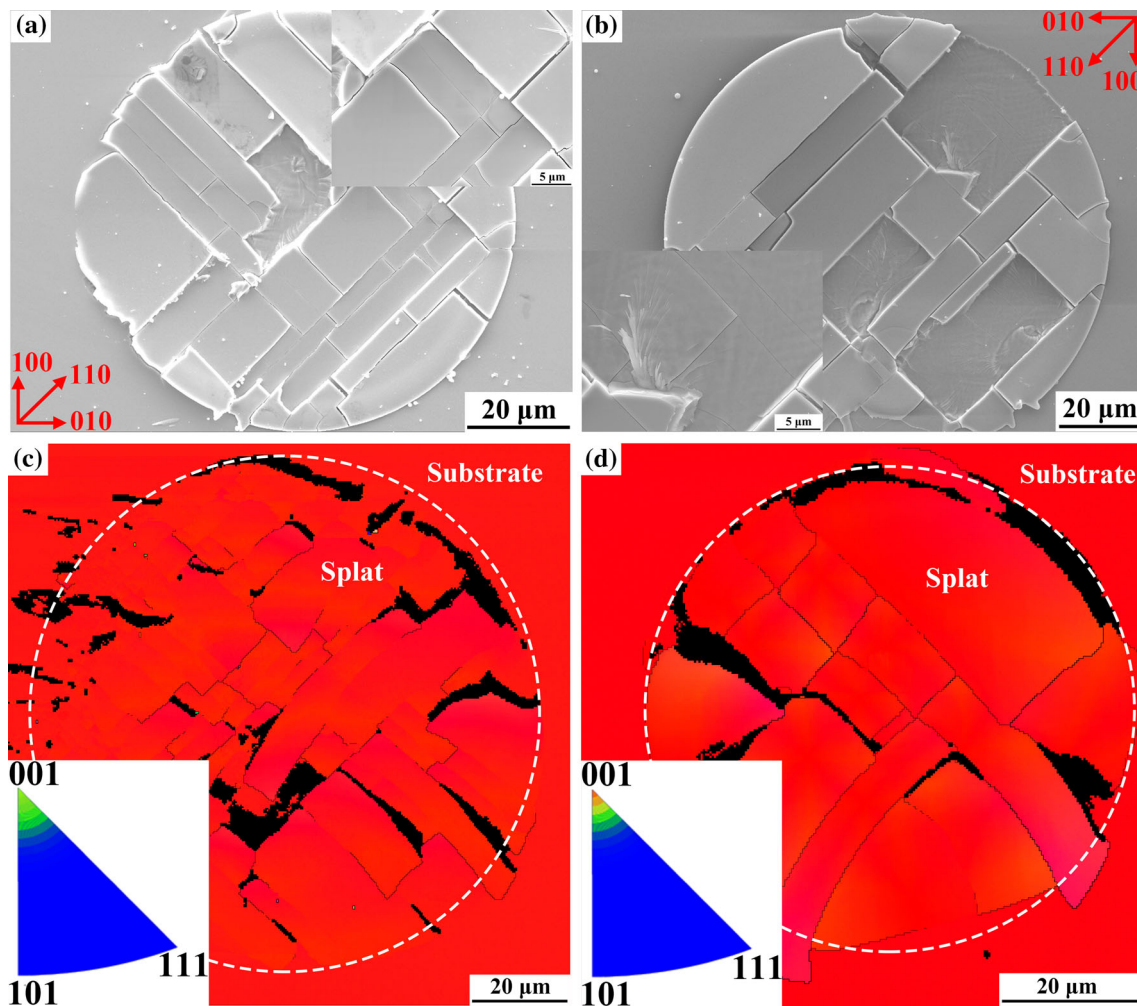


**Fig. 4** Surface morphologies of the LZ film on the single-crystal YSZ substrate at deposition temperatures of (a) 300 °C and (b) 600 °C. The insets in (a) and (b) correspond to high magnification. The red arrows in (a) and (b) represent the crystal directions. The orientation maps of LZ films at deposition temperatures of (c) 300 °C

and (d) 600 °C by EBSD. The insets in (c) and (d) correspond to inverse pole figures (IPFs). The red color and IPFs in EBSD patterns represent the  $\langle 001 \rangle$  orientation. The identical color between film and single-crystal substrate clearly reveals the epitaxial growth has successfully occurred (Color figure online)

and  $1.08 \pm 0.21\%$  for deposition temperatures of 300 and 600 °C, respectively.

Generally, homoepitaxial interfaces should be commensurate and free of net dislocations and physical strains due to the perfect lattice match between the film and substrate, as shown in Fig. 1(a). However, the net dislocations at the homoepitaxial interface in this study depict an anomalous incommensurate interface. To the best of our knowledge, this is the first report on the incommensurate homoepitaxial interfaces to date.

### Statistics of Dislocations at Heteroepitaxial LZ Interfaces

The heteroepitaxial LZ interfaces were also explored by a Cs-corrected HR-TEM, as shown in Fig. 6. The film was about 800–1000 nm thick (see Fig. 8c and d in

“Appendix”). As expected, distinct interface contrasts due to the existing defects were observed at the heteroepitaxial interface, as shown in Fig. 6(a), (b), (e) and (f). Similar to the case of YSZ splats, we first conducted FFT for the HR-TEM images and then IFFT only for the diffraction spot with  $g = [220]$ , as shown in Fig. 9 in “Appendix”. A fair number of defects at the interface were observed, as shown in Fig. 6(d) and (h). Except for the stacking faults, many edge dislocations (marked by red signs) with a Burgers vector of  $(a/2)\langle 110 \rangle$  presented in the interfacial region (marked by two pink dashed lines). To determine the net dislocations along the interfaces, 30 high-magnified images with a total interface length of about 410 nm were counted. It was found that considerable net dislocations existed in the interfacial region corresponding to the distinct interface contrasts, i.e.,  $6.00 \pm 0.40$  and  $5.69 \pm 0.27\%$  for deposition temperatures of 300 and 600 °C, respectively.

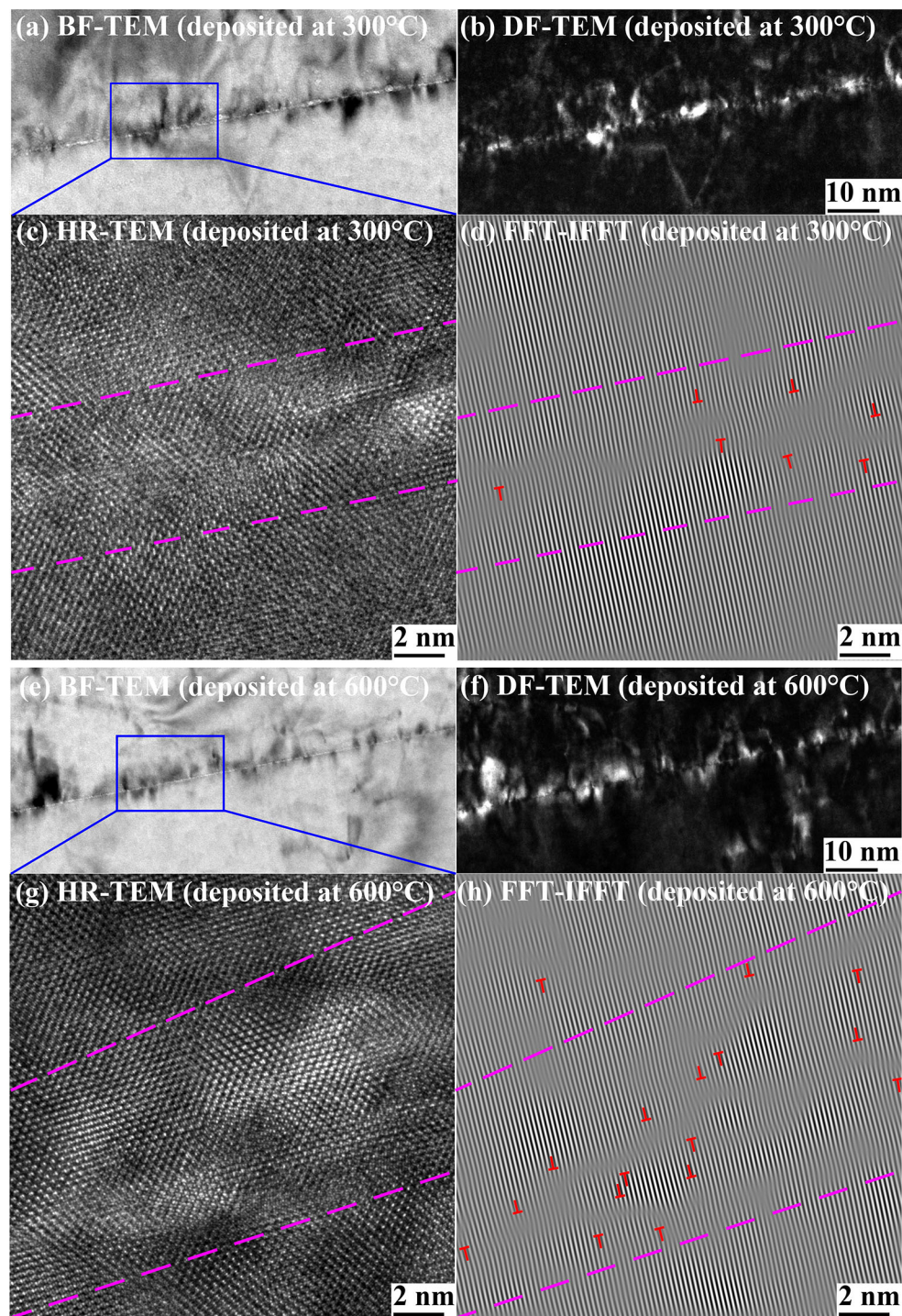


**Fig. 5** Microstructure and quantitative characterization of the homoepitaxial YSZ-YSZ interface. (a) BF-TEM, (b) DF-TEM, (c) HR-TEM and (d) [220] FFT-IFFT images of the film deposited at 300 °C. (e) BF-TEM, (f) DF-TEM, (g) HR-TEM and (h) [220]

FFT-IFFT images of the film deposited at 600 °C. The interface region is marked by two pink dashed lines. The dislocations in (d) and (h) are marked by the red signs (Color figure online)

For single-crystal YSZ and LZ, the lattice parameter at room temperature is 0.5141 and 0.5396 nm, respectively. It can be calculated that the total strain due to

the lattice mismatch between perfectly heteroepitaxial LZ film and YSZ substrate is about 4.72%, which is shared by the defects and physical elastic strain. As a

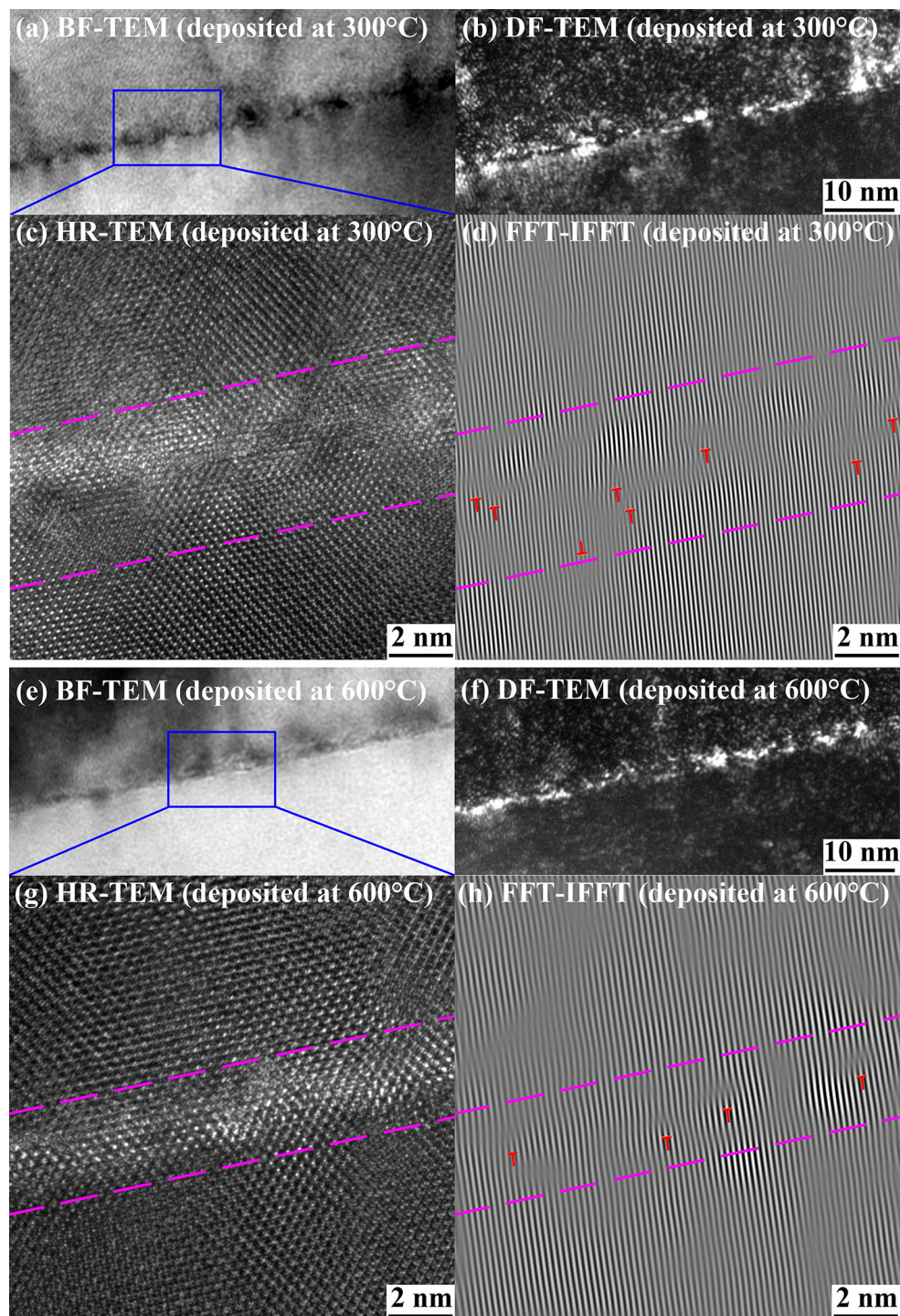


**Fig. 6** Microstructure and quantitative characterization of the heteroepitaxial LZ-YSZ interface. (a) BF-TEM, (b) DF-TEM, (c) HR-TEM and (d) [220] FFT-IFFT images of the film deposited at 300 °C. (e) BF-TEM, (f) DF-TEM, (g) HR-TEM and (h) [220]

FFT-IFFT images of the film deposited at 600 °C. The interface region is marked by two pink dashed lines. The dislocations in (d) and (h) are marked by the red signs (Color figure online)

result, the elastic strain is about  $1.28 \pm 0.40$  and  $0.97 \pm 0.27\%$  for deposition temperatures of 300 and 600 °C, respectively.

In the conventional heteroepitaxial growth of thick film such as by molecular beam epitaxy, the lattice mismatch is almost totally relaxed by the defects, and the physical



elastic strain only comes from thermal expansion mismatch. Taking heteroepitaxial LZ film on YSZ substrate as an example, the physical elastic strain from thermal expansion mismatch with 1000 °C temperature difference yields  $\sim 0.12\%$ . Obviously, it is an anomalous heteroepitaxy which produces excess defects and physical strains in the present study.

## Discussion

### Formation Mechanism of Dislocations and Cracking

As we know, the powder is generally heated to its melting temperature by plasma flow becoming molten droplet during thermally sprayed deposition. From the epitaxial growth perspective, thermally sprayed deposition is an essentially liquid-phase epitaxial process in the present study. However, anomalous dislocations and physical strains were substantially produced in both homoepitaxial YSZ and heteroepitaxial LZ interfacial regions. Apparently, the anomalous epitaxial growths are related to the deposition processing. Herein, the anomalous YSZ homoepitaxy is elaborated. During the thermally sprayed

deposition, the epitaxial film formation goes through five stages, as shown in Fig. 7. Firstly, the molten droplet heated and accelerated by plasma torch impacts the substrate with a high velocity ( $\sim 75$  m/s) (Ref 41, 42), as shown in Fig. 7(I). Then, the droplet rapidly spreads on the substrate forming a liquid film, as shown in Fig. 7(II). During the third stage, the solidification/epitaxial growth starts, and the liquid film transforms into a solid epitaxial film on the single-crystal substrate, as shown in Fig. 7(III). It was reported that the spreading velocity was much larger than cooling rate (Ref 41, 42); therefore, it was reasonable to treat the spreading and solidification process separately. After epitaxial growth, the film together with the substrate rapidly cooled down to room temperature, as shown in Fig. 7(IV). Finally, an epitaxial film bonded on the single-crystal substrate was observed, as shown in Fig. 7(V).

Obviously, dislocations and cracking formed during either solidification or cooling process. It was widely accepted that the cracking was mainly due to the quenching stress (Ref 17–19). Moreover, the vertical cracks in the present study were always oriented along  $\langle 110 \rangle$  directions (generally, the cleavage directions of FCC structures), which again revealed that the vertical cracks were due to the enormous tensile stress. Apparently, the film can be

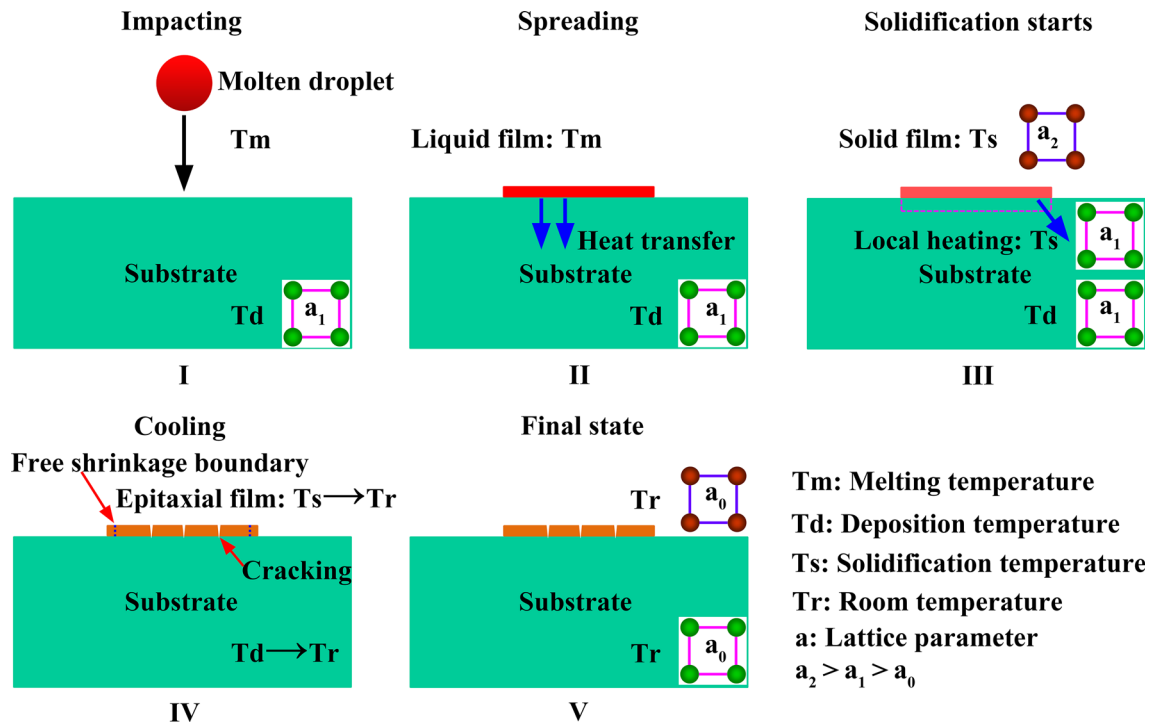


**Fig. 7** Detailed film formation process during the present liquid homoepitaxy by thermal spray technology. A molten droplet with high speed impacts on single-crystal substrate surface (I). The droplet quickly spreads on the substrate forming a liquid film (II). The liquid film starts solidification on substrate forming a solid epitaxial film (III). During the subsequent cooling, the epitaxial film would shrink

with the temperature from  $T_s$  to  $T_r$  (IV). An epitaxial film/substrate system was formed at room temperature (V). The blue dashed line in epitaxial film in (IV) denotes the position in the case of free shrinkage. Additionally, the sign,  $a$ , is the theoretical lattice parameter of the epitaxial film or single-crystal substrate (Color figure online)

considered quasi-liquid during film solidification. In this condition, the film has no strength and cannot sustain any stress. Therefore, it can be stated that cracking mainly forms during the cooling process. However, it is another case for dislocation formation. Compared with conventional epitaxy (Ref 43–45), the dislocation density is much higher in the present epitaxy. Generally, the dislocation nucleation in solid film is hard and slow. However, the thermally sprayed deposition is extremely rapid and only of 10–40  $\mu\text{s}$  (Ref 41, 42). Therefore, it can be stated that explosively formed dislocations mainly formed during the solidification process.

Firstly, an emphasis was placed on the solidification. During film spreading and solidification, the lattice parameter of the film decreased with the temperature dropping. However, since the substrate was much larger than the film in all three dimensions, the substrate worked as a vast reservoir. As a result, the temperature in the whole substrate (except the region covered by the molten film) remained nearly unchanged. As expected, the localized substrate covered by molten film was significantly heated during film spreading and solidification process, but the expansion of this region was strongly constrained by its cold surroundings, as shown in Fig. 7(III). As stated before, there were two types of strain components: one was physical elastic strain and the other was intrinsic caused by thermal field, etc. This kind of intrinsic strain did not produce stress in free condition. Based on the definition in elasticity (Ref 40), the total strain was only related to the displacement change. Obviously, the total strain in localized substrate was nearly zero during solidification, as shown in Fig. 7(III). As a result, enormous compressive physical strain was accumulated in this locally heated substrate to negate the intrinsic thermal strain. Consequently, the lattice parameter of the film was larger than that of this locally heated substrate during the epitaxial growth. However, a liquid-phase homoepitaxial growth on this locally heated region would preferentially form a coherent interface. In this case, the coherent growth on the strained substrate meant that the newly grown solid film also sustained a large compressive strain. However, any solidification process tended to preferentially form a stress-free epitaxial film. As a result, net dislocations were produced in the interfacial layer to negate the lattice mismatch at the film-substrate interface. At last, it was interesting to realize that cracking in the epitaxial film would not happen during epitaxial growth since enormous physical compressive strain was accumulated in the epitaxial film.

After epitaxial growth, the film together with the substrate would rapidly cool down to room temperature, as shown in Fig. 7(IV). However, the degree of thermal shrinkage between the film and substrate was significantly different. The temperature change in epitaxial film during

cooling was from  $T_s$  to  $T_r$  (where  $T_s$  and  $T_r$  were solidification and room temperatures, respectively), while it was actually only from  $T_d$  to  $T_r$  (where  $T_d$  was deposition temperature, 300 or 600  $^{\circ}\text{C}$ ) for the corresponding substrate, as shown in Fig. 7(IV). Compared with free shrinkage (marked by blue dashed lines in Fig. 7(IV)), a large tensile stress in epitaxial film was produced due to the constraints of the substrate. Once the stress in film exceeds its tensile strength, cracking would take place. Taking the elastic modulus of 205 GPa and solidification temperature of 2000  $^{\circ}\text{C}$  (Ref 14) for the YSZ splats into account, the maximum tensile stress in the splats could be as high as  $\sim 2.96$  GPa. Therefore, vertical cracks inevitably occurred to relax this large tensile stress. Furthermore, the cracking direction could be predicted to be along the  $\langle 110 \rangle$  directions, since the  $\langle 110 \rangle$  directions had the severest lattice distortion for this FCC structure and was generally the cleavage directions of FCC structures. The prediction was well consistent with the cracking behavior shown in Fig. 3(a) and (b). In addition, the mean crack spacing slightly increased with an increase in the deposition temperature because of the corresponding decreases in tensile stress.

In brief, large quantities of dislocations were produced during solidification process, while cracking occurred during cooling process. Both of them were due to the constraint effect of cold surroundings on the locally heated substrate. The locally heated substrate with unchanged lattice parameter is the essential difference between conventional homoepitaxy and present liquid-phase homoepitaxy. Ideally, the homoepitaxial film/substrate system is in strain-free state at room temperature. This means the physical tensile strain in epitaxial film during cooling is comparable with the physical compressive strain in film relaxed by dislocations during solidification process. Similar to the case with YSZ, anomalous and redundant dislocations and physical strains were also produced in heteroepitaxial LZ films.

### Relaxation Mechanism of Strain by Dislocations in the Interfacial Region

The strain relaxation mechanisms observed in highly strained epitaxial films generally include relaxation by plastic deformation (such as by dislocations and stacking faults), cracking and surface roughening during the conventional epitaxial growth process (Ref 43–47). Whether or not any mechanism occurs in a given system is determined by a number of factors, among which the lattice mismatch at the film-substrate interface is a crucial one. First, strain relaxation takes place by defects such as the dislocations and stacking faults along the film/substrate interface (Ref 48–51). In this case, the defects have to go through the

whole interface and reach the exterior of this crystalline region at least in one direction. Considering that all stacking faults are local and have small sizes of  $<3$  nm, thus only dislocations should be considered. Second, relaxation by cracking is commonly observed in highly strained heterostructures in tension (Ref 52–54). This mechanism can be ignored in this study, because the strain in the film was compressive during the epitaxial growth process, as shown in Fig. 7(III). Third, the relaxation of purely elastic stresses results in the development of surface undulations (Ref 55–57). This mechanism also can be ignored in this study, since the films presented a very smooth surface profile, see Fig. 3 and 4. In brief, forming dislocations is the only effective mechanism to compensate the apparent lattice mismatch at the film-substrate interface during the solidification process.

Generally, the critical strain required to induce dislocations at the film-substrate interface is about 0.30% (Ref 44). In present study, this critical strain was nearly the same as the error bar of the strain relaxed by dislocations. Consequently, the dislocation concentration data can reveal the true strain at the film-substrate interface. As a result, we can also quantitatively deduce the interface/solidification temperature ( $T_s$ ) during the epitaxy using the strain relaxed by dislocations as follows:

$$T_s = T_d + \frac{\varepsilon_d}{\alpha} \quad (\text{Eq 1})$$

where  $\varepsilon_d$  is the strain relaxed by dislocations and  $\alpha$  is the coefficient of thermal expansion (CTE). The CTE of YSZ and LZ film is about  $10.3 \times 10^{-6}$  and  $9.1 \times 10^{-6}/\text{K}$ , respectively. As a result, the interface/solidification temperature of YSZ films during the epitaxy was found to be  $1630 \pm 282$  and  $1648 \pm 204$  °C for the deposition temperatures ( $T_d$ ) of 300 and 600 °C, respectively. The interface/solidification temperature of LZ films during the epitaxy was  $1706 \pm 440$  and  $1666 \pm 297$  °C for the deposition temperatures of 300 and 600 °C, respectively. Up to now, it is impossible to experimentally measure the solidification temperature in liquid-phase epitaxy (by thermal spray technique) mainly because of the remarkably short solidification time (generally microseconds). However, the interface dislocation density calculated in this study potentially opens a door to determine the interface epitaxial/solidification temperature.

Note that dislocation initiation was a thermal activation process because of large energy barriers. The activation energy of a perfect dislocation in this study was estimated to be 8.59 eV, which was calculated on the basis of the literature (Ref 45, 58–61). The free energy available of 50 kT (where  $k$  is Boltzmann constant) from thermal fluctuation at the typical solidification temperature ( $T$ , about 2000 K) was estimated to be 8.62 eV (Ref 45, 60), i.e., comparable with

the activation energy. As a result, the formation of dislocations became extremely easy during the solidification process. Therefore, the formation of many positive and negative dislocations could be interpreted as follows.

Severe thermal fluctuations result in the formation of larger quantities of dislocations. Additionally, note that the epitaxial growth by thermally sprayed technique is a rapid non-equilibrium process. The cooling rate of the films can be as large as  $10^4$ – $10^6$  K/s (Ref 62). In this case, the thermal energy may spread in the form of thermal waves. As a result, the molten films are turbulent because of severe thermal fluctuations. These wave-like thermal fluctuations result in the formation of high-density dislocations including both positive and negative dislocations. Concomitantly, a fair number of stacking faults arise to alleviate the local high strains between the dislocation pairs. In addition, rapid cooling probably prohibits the annihilation and climb of these supersaturated dislocations. As a result, super-high-density dislocations are retained and observed at room temperature. In brief, both large lattice mismatch and sufficient thermal fluctuation create high-density dislocations. Therefore, the anomalous incommensurate homoepitaxy in this study can also be regarded as a pseudo-heteroepitaxy because of the intrinsic lattice mismatch at the film/substrate interface resulting from the strong constraints on locally heated substrate by its cold surroundings. Conceptually, it seems feasible to regulate the quantities of defects and strains in conventional epitaxial techniques by artificially imposing a pre-strain in the substrate during the epitaxy (Ref 63–65).

### Weak Bonding at LZ/YSZ Interfaces

Apparently, the high-density dislocations lead to weak-bonded interfaces. The severer deterioration would take place in heteroepitaxial interfaces such as between LZ film and YSZ substrate. Firstly, because of enormous lattice mismatch, the density of intrinsic defects such as net dislocations is quite high in the LZ/YSZ interfacial region. Besides, because of extremely rapid cooling rates, the defects from violent thermal fluctuations are extremely high in the interfacial region. Consequently, super-high-density dislocations are produced in the LZ/YSZ interfacial region. This may be the reason for the interface delamination of LZ splats regardless of its epitaxial growth at deposition temperature of 300 °C.

In addition, it should be noted that these high-density dislocations arise in single-crystal/epitaxial films in the present study. The densities in general polycrystalline coatings must be much higher. These interfacial defects significantly contribute to interface cracking and may be the essential formation mechanism of lamellar pores in thermally sprayed coatings.

## Conclusions

In the present study, to investigate the microstructures and defect features at thermally sprayed coating interfaces, the interfaces of the homoepitaxial YSZ and heteroepitaxial LZ films were examined by HR-TEM in detail. It was found, for the first time, large numbers of excess net dislocations in the interfacial region, leading to an anomalous incommensurate homoepitaxial growth in YSZ splats. An anomalous heteroepitaxial growth in LZ splats was also observed. The mechanism of the anomalous incommensurate and heteroepitaxial growth was discussed in detail. Essentially, it is pseudo-heteroepitaxy in YSZ homoepitaxy resulting from the lattice mismatch between the film and substrate which in turn results from the strong constraints on the substrate by the surroundings. In addition, this anomalous lattice mismatch leads to enormous physical strain during the cooling process. The physical strain in YSZ films can be as large as  $1.37 \pm 0.29$  and  $1.08 \pm 0.21$  for the deposition temperatures of 300 and 600 °C, respectively. And this is in LZ films as large as  $1.28 \pm 0.40$  and  $0.97 \pm 0.27$  for the deposition temperatures of 300 and 600 °C, respectively. The solidification temperature was also deduced from the physical strain. It was estimated to be  $1630 \pm 282$  and  $1648 \pm 204$  °C for YSZ films deposited at 300 and 600 °C,

and  $1706 \pm 440$  and  $1666 \pm 297$  °C for LZ films deposited at 300 and 600 °C, respectively.

Moreover, the super-high-density dislocations were ubiquitous in the interfacial region, which were found to result from sufficient thermal fluctuations and extremely rapid cooling rates. Both the anomalous lattice mismatch and super-high-density dislocations lead to weak interfaces and violent cracking in thermally sprayed coatings. These were also the essential differences between conventional and present epitaxy by thermal spray technique. All of these reveal that the essential approach to promoting the performances of thermally sprayed coatings such as LZ/YSZ double-layer TBCs is how to tailor the defects and strains at coating interfaces.

**Acknowledgments** This work is supported by National Basic Research Program (Nos. 2013CB035701), the Fundamental Research Funds for the Central Universities and the National Program for Support of Top-notch Young Professionals. Authors would like to thank Engineer Chuan-sheng Ma for his help with manipulation of TITAN.

## Appendix

The macrostructure and FFT-IFFT processing of epitaxial film (see Fig. 8 and 9).

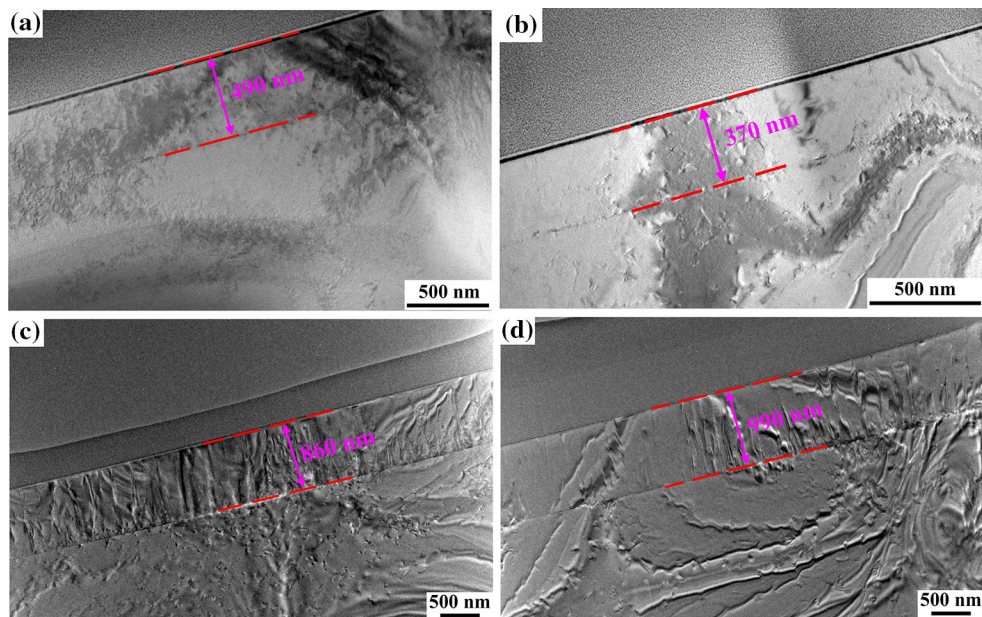


**Fig. 8** Low-magnification microstructures of (a, b) YSZ and (c, d) LZ splats at the deposition temperatures of (a, c) 300 and (b, d) 600 °C, respectively. The film/substrate interfaces are clearly

distinguished. The thickness of YSZ splats was about 300–500 nm (a, b), and this was about 800–1000 nm for LZ splats (c, d)

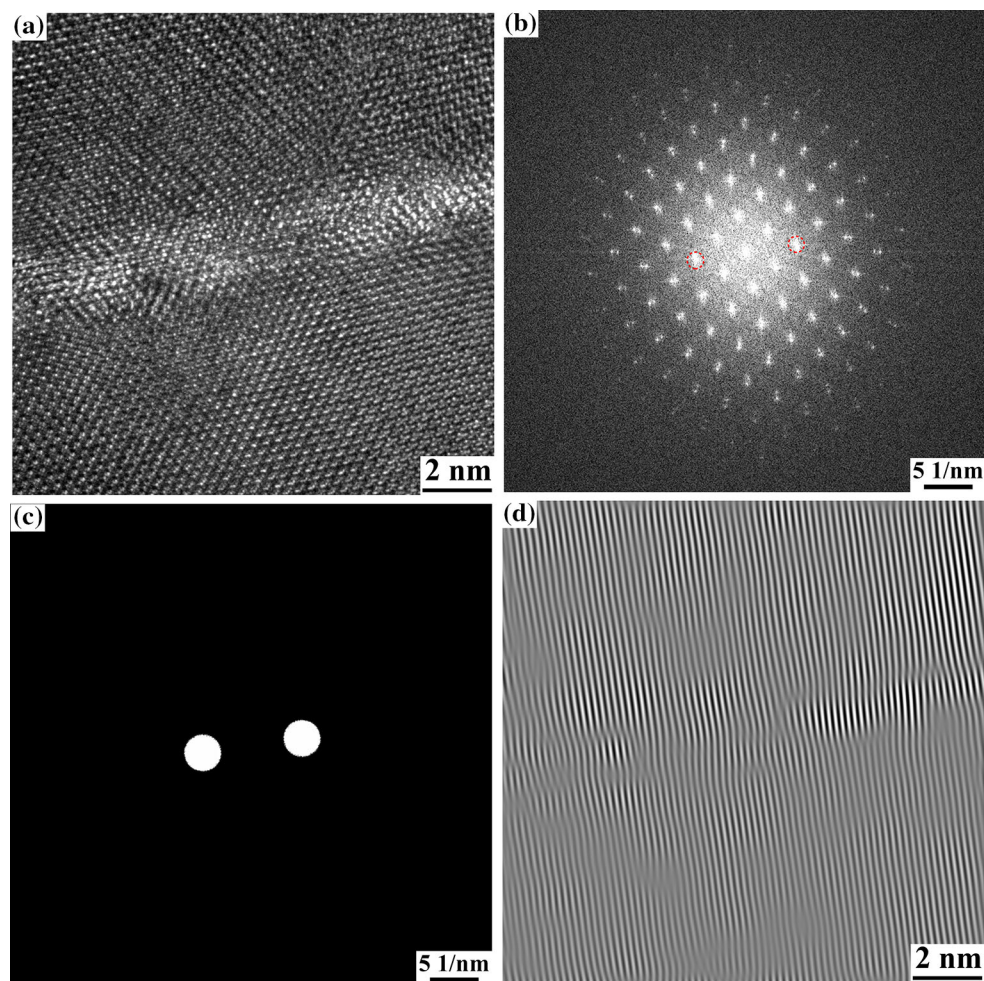


**Fig. 9** FFT and IFFT processing for LZ splat deposited at 300 °C. (a) An original HR-TEM image; (b) FFT image of the region shown in (a); (c) only the spot with [220] direction [the red circle in (b)] was selected; (d) IFFT image of the region shown in (c) (Color figure online)

## References

1. N.P. Padture, M. Gell, and E.H. Jordan, Materials Science—Thermal Barrier Coatings for Gas-Turbine Engine Applications, *Science*, 2002, **296**(5566), p 280-284
2. N.P. Padture, Advanced Structural Ceramics in Aerospace Propulsion, *Nat. Mater.*, 2016, **15**(8), p 804-809
3. Y.Z. Xing, C.J. Li, C.X. Li, and G.J. Yang, Influence of Through-Lamella Grain Growth on Ionic Conductivity of Plasma-Sprayed Ytria-Stabilized Zirconia as an Electrolyte in Solid Oxide Fuel Cells, *J. Power Sources*, 2008, **176**(1), p 31-38
4. G. Bolelli, V. Cannillo, L. Lusvardi, and T. Manfredini, Wear Behaviour of Thermally Sprayed Ceramic Oxide Coatings, *Wear*, 2006, **261**(11–12), p 1298-1315
5. S. Wilson, Thermally Sprayed Abradable Coating Technology for Sealing in Gas Turbines. In: *6th International Conference on the Future of Gas Turbine Technology* (2012)
6. E. Irissou, A. Dadouche, and R.S. Lima, Tribological Characterization of Plasma-Sprayed CoNiCrAlY-BN Abradable Coatings, *J. Therm. Spray Technol.*, 2014, **23**(1–2), p 252-261
7. D. Sporer, M. Dorfman, L. Xie, A. Refke, I. Giovannetti, and M. Giannozzi, Processing and Properties of Advanced Ceramic Abradable Coatings, *Therm. Spray Glob. Coat. Solut.*, 2007, **2007**, p 14-16
8. H. Dong, G.J. Yang, H.N. Cai, C.X. Li, and C.J. Li, Propagation Feature of Cracks in Plasma-Sprayed YSZ Coatings Under Gradient Thermal Cycling, *Ceram. Int.*, 2015, **41**(3), p 3481-3489
9. C.J. Li, Y. Li, G.J. Yang, and C.X. Li, Evolution of Lamellar Interface Cracks During Isothermal Cyclic Test of Plasma-Sprayed 8YSZ Coating with a Columnar-Structured YSZ Interlayer, *J. Therm. Spray Technol.*, 2013, **22**(8), p 1374-1382
10. S. Ahmadian and E.H. Jordan, Explanation of the Effect of Rapid Cycling on Oxidation, Rumpling, Microcracking and Lifetime of Air Plasma Sprayed Thermal Barrier Coatings, *Surf. Coat. Technol.*, 2014, **244**, p 109-116
11. B. Cheng, Y.M. Zhang, N. Yang, M. Zhang, L. Chen, G.J. Yang, C.X. Li, and C.J. Li, Sintering-Induced Delamination of Thermal Barrier Coatings by Gradient thermal Cyclic Test, *J. Am. Ceram. Soc.*, 2017, doi:[10.1111/jace.14713](https://doi.org/10.1111/jace.14713)
12. J.P. Schaffer, *The Science and Design of Engineering Materials*, 2nd ed., Higher Education Press, Beijing, 2003
13. T. Chraska and A.H. King, Effect of Different Substrate Conditions upon Interface with Plasma Sprayed Zirconia—A TEM Study, *Surf. Coat. Technol.*, 2002, **157**(2–3), p 238-246

14. T. Chraska and A.H. King, Transmission Electron Microscopy Study of Rapid Solidification of Plasma Sprayed Zirconia—Part I. First Splat Solidification, *Thin Solid Films*, 2001, **397**(1–2), p 30-39
15. T. Chraska and A.H. King, Transmission Electron Microscopy Study of Rapid Solidification of Plasma Sprayed Zirconia—Part II. Interfaces and Subsequent Splat Solidification, *Thin Solid Films*, 2001, **397**(1–2), p 40-48
16. E.J. Yang, X.T. Luo, G.J. Yang, C.X. Li, and C.J. Li, A TEM Study of the Microstructure of Plasma-Sprayed YSZ Near Inter-Splat Interfaces, *J. Therm. Spray Technol.*, 2015, **24**(6), p 907-914
17. S. Kuroda and T.W. Clyne, The Quenching Stress in Thermally Sprayed Coatings, *Thin Solid Films*, 1991, **200**(1), p 49-66
18. S. Kuroda, T. Fukushima, and S. Kitahara, Significance of Quenching Stress in the Cohesion and Adhesion of Thermally Sprayed Coatings, *J. Therm. Spray Technol.*, 1992, **1**(4), p 325-332
19. S. Kuroda, T. Dendo, and S. Kitahara, Quenching Stress in Plasma-Sprayed Coatings and its Correlation with the Deposit Microstructure, *J. Therm. Spray Technol.*, 1995, **4**(1), p 75-84
20. S.B. Wang, L. Pan, J.J. Song, W.B. Mi, J.J. Zou, L. Wang, and X.W. Zhang, Titanium-Defected Undoped Anatase TiO<sub>2</sub> with p-Type Conductivity, Room-Temperature Ferromagnetism, and Remarkable Photocatalytic Performance, *J. Am. Chem. Soc.*, 2015, **137**(8), p 2975-2983
21. F. Zuo, L. Wang, T. Wu, Z.Y. Zhang, D. Borchardt, and P.Y. Feng, Self-doped Ti<sup>3+</sup> Enhanced Photocatalyst for Hydrogen Production Under Visible Light, *J. Am. Chem. Soc.*, 2010, **132**(34), p 11856-11857
22. X. Zhu, K.L. Mills, P.R. Peters, J.H. Bahng, E.H. Liu, J. Shim, K. Naruse, M.E. Csete, M.D. Thouless, and S. Takayama, Fabrication of Reconfigurable Protein Matrices by Cracking, *Nat. Mater.*, 2005, **4**(5), p 403-406
23. D. Huh, K.L. Mills, X.Y. Zhu, M.A. Burns, M.D. Thouless, and S. Takayama, Tuneable Elastomeric Nanochannels for Nanofluidic Manipulation, *Nat. Mater.*, 2007, **6**(6), p 424-428
24. B.C. Kim, C. Moraes, J. Huang, M.D. Thouless, and S. Takayama, Fracture-Based Micro- and Nanofabrication for Biological Applications, *Biomater. Sci.*, 2014, **2**(3), p 288-296
25. P. Kim, M. Abkarian, and H.A. Stone, Hierarchical Folding of Elastic Membranes Under Biaxial Compressive Stress, *Nat. Mater.*, 2011, **10**(12), p 952-957
26. Y. Gao, Q.C. Liu, and B.X. Xu, Lattice Mismatch Dominant Yet Mechanically Tunable Thermal Conductivity in Bilayer Heterostructures, *ACS Nano*, 2016, **10**(5), p 5431-5439
27. J. Garcia-Barriocanal, A. Rivera-Calzada, M. Varela, Z. Sefrioui, E. Iborra, C. Leon, S.J. Pennycook, and J. Santamaria, Colossal Ionic Conductivity at Interfaces of Epitaxial ZrO<sub>2</sub>: Y<sub>2</sub>O<sub>3</sub>/SrTiO<sub>3</sub> Heterostructures, *Science*, 2008, **321**(5889), p 676-680
28. R. Adelung, O.C. Aktas, J. Franc, A. Biswas, R. Kunz, M. Elbahri, J. Kanzow, U. Schurmann, and F. Faupel, Strain-Controlled Growth of Nanowires within Thin-Film Cracks, *Nat. Mater.*, 2004, **3**(6), p 375-379
29. M. De Volder, S. Park, S. Tawfick, and A.J. Hart, Strain-Engineered Manufacturing of Freeform Carbon Nanotube Microstructures, *Nat. Commun.*, 2014, doi:10.1038/ncomms5512
30. S.A. Campbell, *The Science and Engineering of Microelectronic Fabrication*, 2nd ed., Oxford University Press Inc., New York, 2001
31. B.A. Joyce, The Epitaxy of Silicon on Alumina—Structural Effects, *Philos. Mag.*, 1966, **14**, p 31-46
32. H.M. Manasevit, A Survey of the Heteroepitaxial Growth of Semiconductor Films on Insulating Substrates, *J. Cryst. Growth*, 1974, **22**(2), p 125-148
33. W.I. Wang, Molecular-Beam Epitaxial-Growth and Material Properties of GaAs and AlGaAs on Si(100), *Appl. Phys. Lett.*, 1984, **44**(12), p 1149-1151
34. W.T. Masselink, T. Henderson, J. Klem, R. Fischer, P. Pearah, H. Morkoç, M. Hafich, P.D. Wang, and G.Y. Robinson, Optical Properties of GaAs on (100) Si Using Molecular Beam Epitaxy, *Appl. Phys. Lett.*, 1984, **45**(12), p 1309-1311
35. Z. Lin, A. Yin, J. Mao, Y. Xia, N. Kempf, Q. He, Y. Wang, C.-Y. Chen, Y. Zhang, and V. Ozolins, Scalable Solution-Phase Epitaxial Growth of Symmetry-Mismatched Heterostructures on Two-Dimensional Crystal Soft Template, *Sci. Adv.*, 2016, **2**(10), p 1-9
36. L. Chen, G.J. Yang, C.X. Li, and C.J. Li, Hierarchical Formation of Intrasplat Cracks in Thermal Spray Ceramic Coatings, *J. Therm. Spray Technol.*, 2016, **25**(5), p 959-970
37. L. Chen, G.-J. Yang, C.-X. Li, and C.-J. Li, Edge Effect on Crack Patterns in Thermally Sprayed Ceramic Splats, *J. Therm. Spray Technol.*, 2016, doi:10.1007/s11666-016-0505-6
38. S. Kaiser, H. Preis, W. Gebhardt, O. Ambacher, H. Angerer, M. Stutzmann, A. Rosenauer, and D. Gerthsen, Quantitative Transmission Electron Microscopy Investigation of the Relaxation by Misfit Dislocations Confined at the Interface of GaN/Al<sub>2</sub>O<sub>3</sub>(0001), *Jpn. J. Appl. Phys.*, 1998, **37**(1), p 84-89
39. J.H. Joo, K.J. Greenberg, M. Baram, D.R. Clarke, and E.L. Hu, Aqueous Epitaxial Growth of ZnO on Single Crystalline Au Microplates, *Cryst. Growth Des.*, 2013, **13**(3), p 986-991
40. S.P.T. Goodier, S.P. Timoshenko, and J.N. Goodier, *Theory of Elasticity*, MacGraw Hill International Book, New York, 1982
41. C. Moreau, P. Cielo, M. Lamontagne, S. Dallaire, J.C. Krapez, and M. Vardelle, Temperature Evolution of Plasma-Sprayed Niobium Particles Impacting on a Substrate, *Surf. Coat. Technol.*, 1991, **46**(2), p 173-187
42. H. Jones, Cooling, Freezing and Substrate Impact of Droplets Formed by Rotary Atomization, *J. Phys. D Appl. Phys.*, 1971, **4**(11), p 1657-1660
43. X. Wu and G.C. Weatherly, The Surface Topography of Cracks in Strained In<sub>0.72</sub>Ga<sub>0.28</sub>P Films, *Philos. Mag. Lett.*, 2000, **80**(8), p 535-541
44. Y. Li, G.C. Weatherly, and M. Niewczas, TEM Studies of Stress Relaxation in GaAsN and GaP Thin Films, *Philos. Mag.*, 2005, **85**(26–27), p 3073-3090
45. X. Wu and G.C. Weatherly, The First Stage of Stress Relaxation in Tensile Strained In<sub>1-x</sub>Ga<sub>x</sub>As<sub>1-y</sub>P<sub>y</sub> Films, *Philos. Mag. A*, 2001, **81**(6), p 1489-1506
46. R.V. Kukta and L.B. Freund, Minimum Energy Configuration of Epitaxial Material Clusters on a Lattice-Mismatched Substrate, *J. Mech. Phys. Solids*, 1997, **45**(11), p 1835-1860
47. X.H. Wu, Strain relaxation in indium gallium arsenide phosphide films on indium phosphide substrates, Ph. D. Thesis, McMaster University, 2000
48. L.B. Freund, The Mechanics of Dislocations in Strained-Layer Semiconductor-Materials, *Adv. Appl. Mech.*, 1994, **30**, p 1-66
49. J.W. Matthews, A.E. Blakeslee, and S. Mader, Use of Misfit Strain to Remove Dislocations from Epitaxial Thin-Films, *Thin Solid Films*, 1976, **33**(2), p 253-266
50. B.C.D. Cooman and C.B. Carter, The Accommodation of Misfit at 100 Heterojunctions in III–V Compound Semiconductors by Gliding Dissociated Dislocations, *Acta Metall.*, 1989, **37**(10), p 2765-2777
51. A.F. Schwartzman and R. Sinclair, Metastable and Equilibrium Defect Structure of II–VI/GaAs Interfaces, *J. Electron. Mater.*, 1991, **20**(7), p 805-814
52. X. Wu and G.C. Weatherly, Cracking Phenomena in In(0.25)Ga(0.75)As Films on InP Substrates, *Acta Mater.*, 1999, **47**(12), p 3383-3394

53. R.T. Murray, C.J. Kiely, and M. Hopkinson, Crack Formation in III-V Epilayers Grown Under Tensile Strain on InP(001) Substrates, *Philos. Mag. A*, 1996, **74**(2), p 383-393
54. M.D. Thouless, E. Olsson, and A. Gupta, Cracking of Brittle Films on Elastic Substrates, *Acta Metall. Mater.*, 1992, **40**(6), p 1287-1292
55. Y. Chen and J. Washburn, Structural Transition in Large-Lattice-Mismatch Heteroepitaxy, *Phys. Rev. Lett.*, 1996, **77**(19), p 4046-4049
56. J. Tersoff and F.K. Legoues, Competing Relaxation Mechanisms in Strained Layers, *Phys. Rev. Lett.*, 1994, **72**(22), p 3570-3573
57. X. Wu and G.C. Weatherly, Composition Modulations in Tensile Strained  $\text{In}_{1-x}\text{Ga}_x\text{As}_y\text{P}_{1-y}$  Films Grown on (100) InP Substrates, *J. Cryst. Growth*, 2001, **233**(1–2), p 88-98
58. S.V. Kamat and J.P. Hirth, Dislocation Injection in Strained Multilayer Structures, *J. Appl. Phys.*, 1990, **67**(11), p 6844-6850
59. P.M.J. Maree, J.C. Barbour, J.F. Vanderveen, K.L. Kavanagh, C.W.T. Bulleliuwma, and M.P.A. Vieggers, Generation of Misfit Dislocations in Semiconductors, *J. Appl. Phys.*, 1987, **62**(11), p 4413-4420
60. J.P. Hirth, J. Lothe, and T. Mura, *Theory of Dislocations*, 2nd ed., John Wiley & Sons, New York, 1982
61. D.J. Eaglesham, E.P. Kvam, D.M. Maher, C.J. Humphreys, and J.C. Bean, Dislocation Nucleation Near the Critical Thickness in GeSi/Si Strained Layers, *Philos. Mag. A*, 1989, **59**(59), p 1059-1073
62. M. Vardelle, A. Vardelle, A.C. Leger, P. Fauchais, and D. Gobin, Influence of Particle Parameters at Impact on Splat Formation and Solidification in Plasma Spraying Processes, *J. Therm. Spray Technol.*, 1995, **4**(1), p 50-58
63. S. Wooh, S. Lee, Y. Lee, J.H. Ryu, W.B. Lee, H. Yoon, and K. Char, Isolated Mesoporous Microstructures Prepared by Stress Localization-Induced Crack Manipulation, *ACS Nano*, 2016, **10**(10), p 9259-9266
64. R.M. Yu, X.F. Wang, W.B. Peng, W.Z. Wu, Y. Ding, S.T. Li, and Z.L. Wang, Piezotronic Effect in Strain-Gated Transistor of a-Axis GaN Nanobelt, *ACS Nano*, 2015, **9**(10), p 9822-9829
65. L. Oakes, R. Carter, T. Hanken, A.P. Cohn, K. Share, B. Schmidt, and C.L. Pint, Interface Strain in Vertically Stacked Two-Dimensional Heterostructured Carbon-MoS<sub>2</sub> Nanosheets Controls Electrochemical Reactivity, *Nat. Commun.*, 2016, doi:[10.1038/ncomms11796](https://doi.org/10.1038/ncomms11796)